TECHNICAL REVIEW

Non-stationary STSF

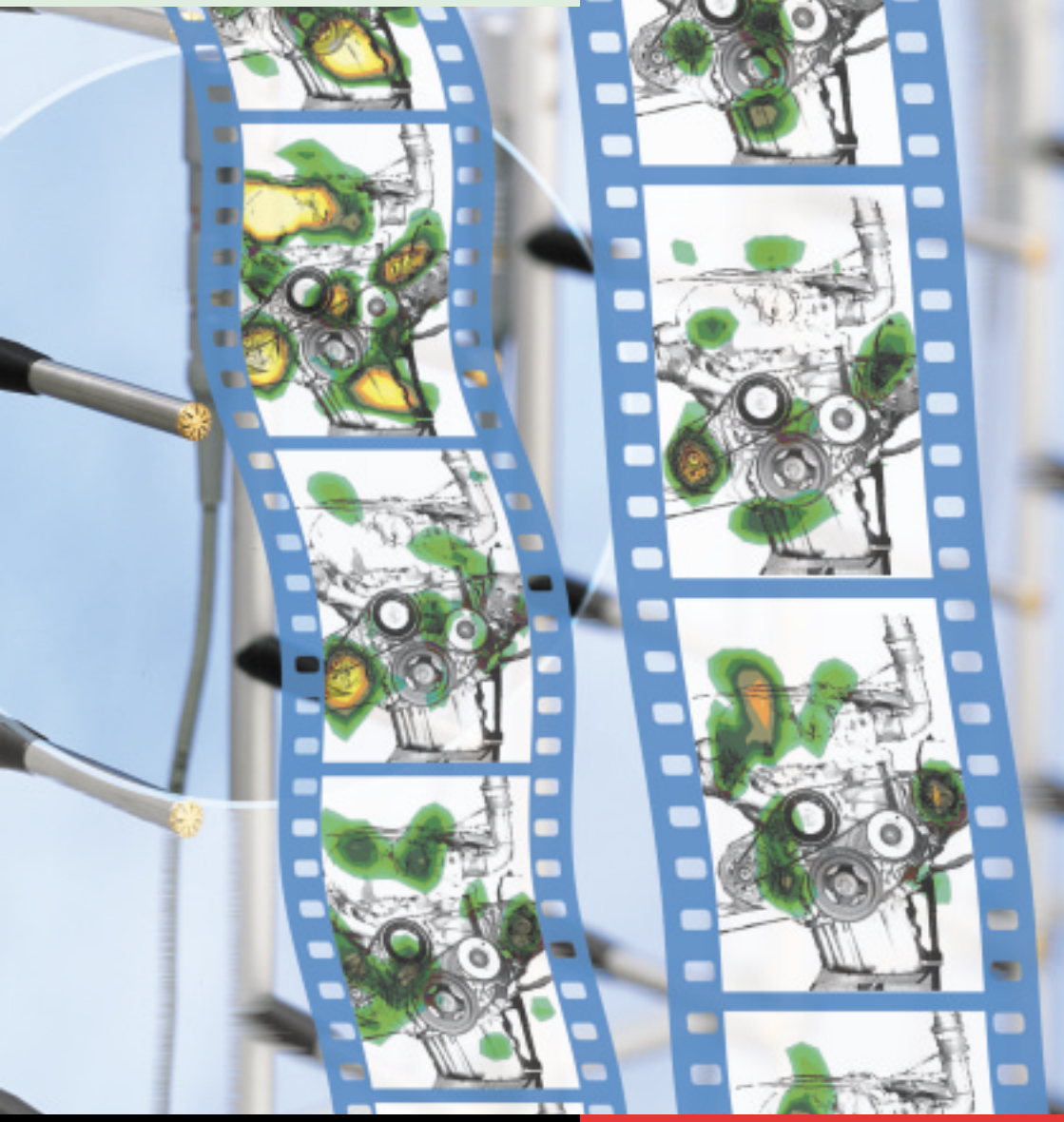

No.1 2000

Brüel & Kjær

Previously issued numbers of Brüel & Kjær Technical Review

1 – 1999 Characteristics of the Vold-Kalman Order Tracking Filter

1 – 1998 Danish Primary Laboratory of Acoustics (DPLA) as Part of the National Metrology Organisation
Pressure Reciprocity Calibration – Instrumentation, Results and Uncertainty
MP.EXE, a Calculation Program for Pressure Reciprocity Calibration of Microphones

1 – 1997 A New Design Principle for Triaxial Piezoelectric Accelerometers
A Simple QC Test for Knock Sensors
Torsional Operational Deflection Shapes (TODS) Measurements

2 – 1996 Non-stationary Signal Analysis using Wavelet Transform, Short-time Fourier Transform and Wigner-Ville Distribution

1 – 1996 Calibration Uncertainties & Distortion of Microphones.
Wide Band Intensity Probe. Accelerometer Mounted Resonance Test

2 – 1995 Order Tracking Analysis

1 – 1995 Use of Spatial Transformation of Sound Fields (STSF) Techniques in the Automative Industry

2 – 1994 The use of Impulse Response Function for Modal Parameter Estimation
Complex Modulus and Damping Measurements using Resonant and Non-resonant Methods (Damping Part II)

1 – 1994 Digital Filter Techniques vs. FFT Techniques for Damping Measurements (Damping Part I)

2 – 1990 Optical Filters and their Use with the Type 1302 & Type 1306 Photoacoustic Gas Monitors

1 – 1990 The Brüel & Kjær Photoacoustic Transducer System and its Physical Properties

2 – 1989 STSF — Practical Instrumentation and Application
Digital Filter Analysis: Real-time and Non Real-time Performance

1 – 1989 STSF — A Unique Technique for Scan Based Near-Field Acoustic Holography Without Restrictions on Coherence

2 – 1988 Quantifying Draught Risk

1 – 1988 Using Experimental Modal Analysis to Simulate Structural Dynamic Modifications
Use of Operational Deflection Shapes for Noise Control of Discrete Tones

4 – 1987 Windows to FFT Analysis (Part II)
Acoustic Calibrator for Intensity Measurement Systems

3 – 1987 Windows to FFT Analysis (Part I)

2 – 1987 Recent Developments in Accelerometer Design
Trends in Accelerometer Calibration

1 – 1987 Vibration Monitoring of Machines

(Continued on cover page 3)

Technical Review

No. 1 – 2000

Contents

Editor: Harry K. Zaveri Photographer: Peter Dalmo

Non-stationary STSF

by J. Hald

Abstract

This article gives a general introduction to the principles and applications of the Brüel & Kjær Non-stationary STSF measurement technique, with special emphasis on the new functionality included with Version 2.0 of the software package Type 7712. After a general introduction, the principles of *Bad Measurement Point Interpolation* and *Envelope Intensity* are descibed. Two case studies of typical applications are then outlined: the first one, which is measurement of brake squeal, is an example of transient noise source localisation. The second case study is mapping and analysis of microphenomena and orders in engine noise radiation.

Résumé

Dans cet article sont présentés les principes et les applications de la technique Brüel & Kjær de mesure STSF pour source non stationnaire. L'accent y est mis sur la nouvelle fonctionnalité incluse à la Version 2.0 du Logiciel 7712. Après une introduction générale, les principes de l'Interpolation de points de mesure erronés et de l'Intensité d'enveloppe y sont décrits, avec deux cas typiques d'application concrète. Le premier, exemple de localisation de source transitoire, est l'analyse d'un crissement de frein. Le second est un exemple de cartographie et d'analyse des ordres et des micro-phénomènes caractérisant l'émission d'un bruit de moteur.

Zusammenfassung

Dieser Artikel gibt eine allgemeine Einführung in Prinzipien und Anwendungen der nichtstationären STSF-Meßtechnik von Brüel & Kjær, wobei besonderes Gewicht auf die neue Funktionalität von Version 2.0 des Softwarepakets Typ 7712 gelegt wird. Nach den Grundlagen werden die Prinzipien der Interpolation für schlechte Meßpunkte und Hüllkurvenintensität beschrieben und anschließend zwei Fallstudien typischer Anwendungen skizziert. Bei der ersten handelt es sich um die Messung des Bremsenquietschens als Beispiel für Schallquellenortung eines transienten Geräuschs. Die zweite beschreibt Kartierung und Analyse von Mikrophänomenen und Ordnungen bei der Schallabstrahlung von Motoren.

Nomenclature

c	Propagation speed of sound
ρ	Density of medium
t	Time
ω	Temporal angular frequency
k	Wave number
$\mathbf{r} = \{x, y, z\}^{\mathrm{T}}$	Rectangular 3D co-ordinates
$\mathbf{R} = \{x,y\}^{\mathrm{T}}$	Rectangular 2D co-ordinates
$\mathbf{k} = \{k_x, k_y, k_z\}^{\mathrm{T}}$	Spatial angular frequencies in 3D
$\mathbf{K} = \{k_x,k_y\}^{\mathrm{T}}$	Spatial angular frequencies in 2D
p	Sound pressure time signal
p_c	Complex analytic pressure time signal
$\widehat{p}$	Hilbert transform of sound pressure time signal p
$\underline{p}$	Pressure in temporal frequency (and spatial) domain
P	Pressure in temporal frequency and spatial frequency domain
$\mathbf{u} = (u_x, u_y,u_z)^{\mathrm{T}}$	Particle velocity time signal vector
$\mathbf{u}_c$	Complex particle velocity time signal vector
$\mathbf{I}$	Instantaneous Intensity vector
$\mathbf{I}_c$	Instantaneous Complex Intensity vector
$\bar{\mathbf{I}}$	Envelope active intensity vector
$\bar{\mathbf{Q}}$	Envelope reactive intensity vector
$\mathbf{c} = \mathbf{a} + j\mathbf{b}$	Vector of complex interpolation coefficients
$W(\mathbf{K})$	Weighting function
E	Interpolation error
J_0, J_1	Bessel functions

Introduction

The measurement principle of Non-stationary STSF (NS-STSF) was developed and applied within a sound field assessment task of the Brite-Euram research project PIANO which ended at the beginning of 1996. The PIANO project was dealing with new methods that enable faster, cheaper, and more accurate ISO 362 pass-by noise reduction measures for heavy road vehicles. These vehicles are invariably operating under transient conditions, requiring laboratory testing under transient conditions. The Cross Spectral STSF implementation of Near-field Acoustical Holography, see [1] and [2], requires stationary signals and therefore did not apply.

NS-STSF is an implementation of Time Domain Holography (TDH) [3]. Because it is a time domain method, all signals need to be measured simultaneously. TDH processes a recorded acoustic event that consists of simultaneously measured pressure time histories from a planar surface covering the sound source. As a consequence, the scan principle used in STSF cannot be used – a full-size microphone array is needed. The two big advantages of NS-STSF are that there are no requirements for stationarity and that full time resolution is retained throughout the NS-STSF measurement and the Time Domain Holography calculations. Thus, while STSF provides detailed information about *where* noise is radiated, NS-STSF can show both *where* and *when* noise is radiated.

This paper briefly describes the principles and the theory of NS-STSF, including the use of *Envelope Intensity* to overview the sometimes very complicated time variations encountered. After that some typical application examples are given.

Principles of NS-STSF

TDH maps all sound field descriptors (pressure, particle velocity, intensity, etc.) in the near field, not only as a function of physical location, but also as a function of time. A TDH measurement can be seen as a sequence of snapshots of the instantaneous pressure over the array area, the time separation between subsequent snapshots being equal to the sampling interval in the A/D conversion. Similarly, the basic output of TDH is a time sequence of snapshots of a selected acoustic quantity in a calculation plane parallel with the measurement plane.

An example is given in Fig.1, which contains a sequence of snapshots of Instantaneous Air Particle Displacement over a calculation plane at the side of a truck tyre.

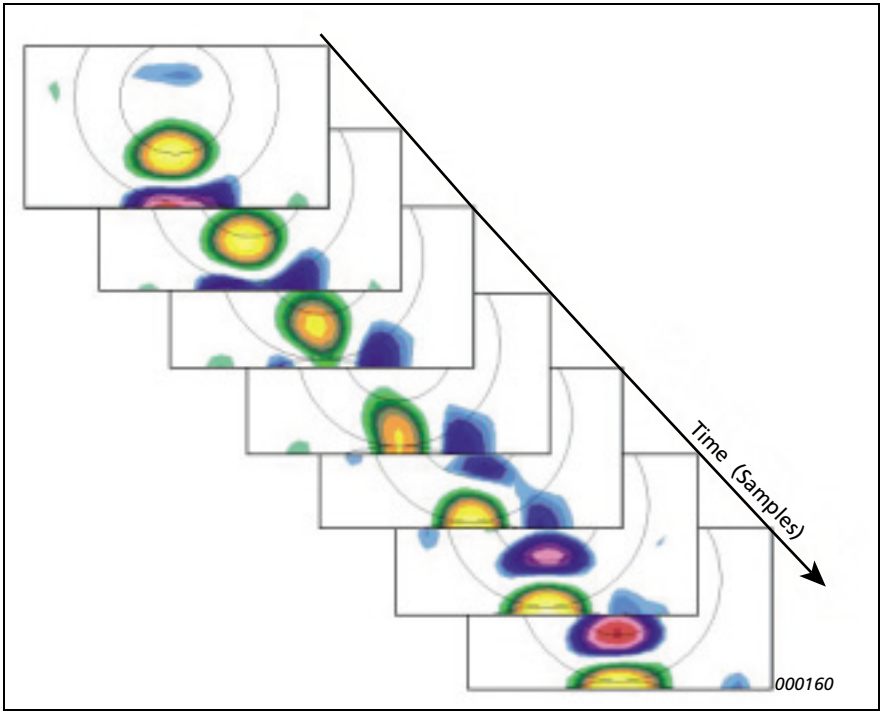

Fig. 1. Illustration of the combined space and time resolution. The maps represent air particle displacement away from a tyre

When NS-STSF is applied for engine noise analysis, two crankshaft tacho signals are normally recorded simultaneous with the array signals – one high resolution tacho for precise measurement of the crank angle rotation, and another for identification of a reference angular position. These two tacho signals allow the crank angle at the time of each snapshot to be identified in addition to the engine RPM. With the NS-STSF system it is therefore possible to visualize radiation and, at the same time, relate it to the different events during an engine cycle.

Fig. 2 shows in schematic form the data flow in NS-STSF. Notice that averaging is an option – it is possible to display with sample rate time resolution.

Sequences of maps can be animated, as illustrated in Fig. 1, to provide a visual understanding of the sound radiation process.

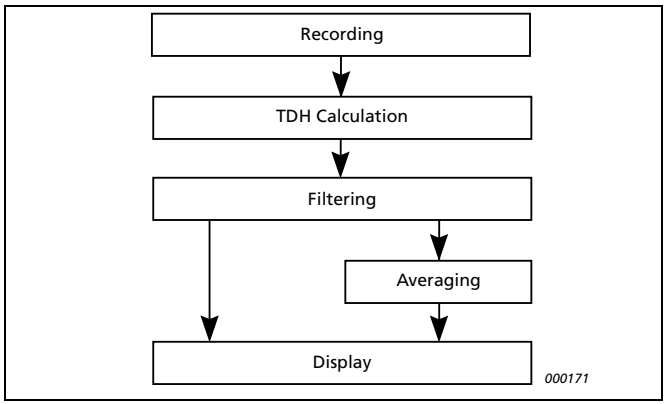

Fig. 2. Data flow in NS-STSF

When no averaging is performed, and the output is time signals, these signals can be exported to any type of post-processing. For example, exported pressure time signals can be used for subjective sound evaluation in the PULSE Sound Quality software Type 7698.

Just like the STSF software Type 7688, the NS-STSF software can also simulate source modification by attenuating a particle velocity map over selected sub-areas of a plane at the source surface. The sound field of the modified source (velocity map) can then be calculated and investigated. For example, pressure time signals at some distance can be calculated and exported for subjective sound evaluation.

Instrumentation

The microphone array consists of a large number of specially designed low-cost Array Microphones Type 4935 that can be clipped into position in an open grid network. Fig. 3 shows an array with 10 columns and 12 rows of microphones fitted into a so-called Integral Connection Array WA 0806. Here, the microphones do not need individual cabling. Instead, groups of six microphones are fitted into a tube with integrated cabling to a single LEMO connector, from where the six microphones are connected with a single cable to the front-end.

The front-end is an Intelligent Data Acquisition (IDA) front-end system Type 3561. Time-history data is stored in real time in the front-end, and after the recording is completed, data is transferred through a standard Ethernet interface to the host computer running the Non-Stationary STSF software Type 7712. The IDA front-end can handle up to 3000 channels in multiple frames.

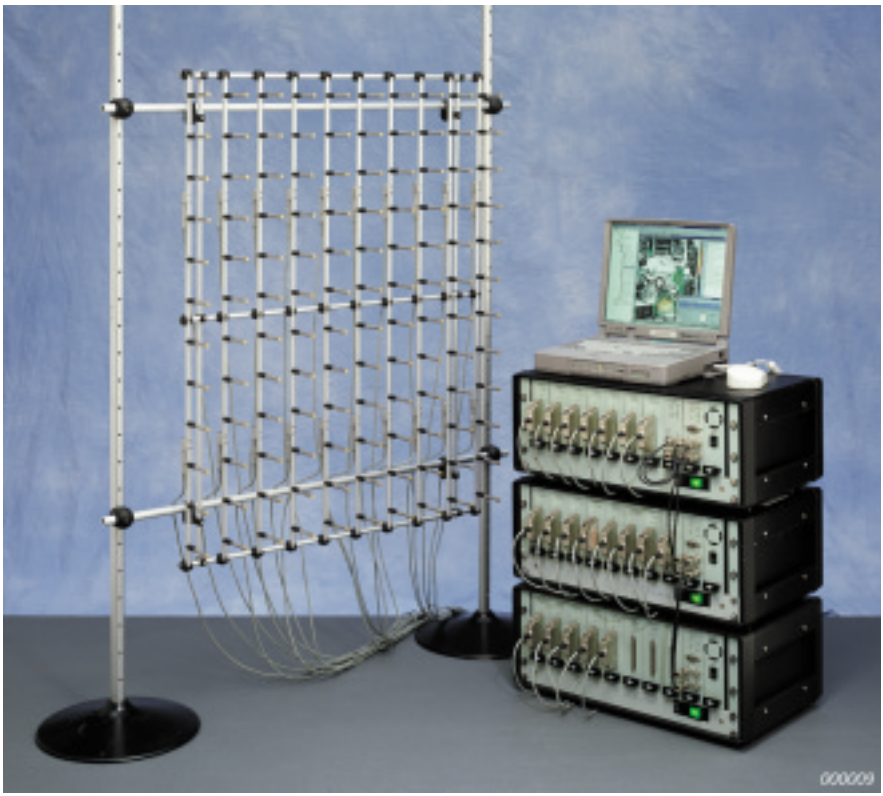

Fig. 3. 120 element microphone array, IDA front-end and computer for NS-STSF

The software includes dedicated functionality to facilitate the handling of the large number of measurement channels often required for the NS-STSF application. For example, a Detect function automates the definition of the

array (*row*, *column*) connections to the front-end channels (*frame*, *module*, and *channel*). Calibration can be performed on six microphones in parallel using a special pistonphone adaptor, and the software automatically detects which channels are being calibrated. Finally, there is extensive on-line monitoring of channel status, reporting for example cable break, CCLD fault and Overload.

Theory of Time Domain Acoustical Holography

Fig. 4 illustrates the geometry of the measurement problem. The sound pressure is measured over a plane $z = z_0 > 0$ in the near-field region of a sound source. All parts of the source are assumed to be in the half space $z < 0$, and the half space $z \geq 0$ is assumed to be source-free and homogeneous.

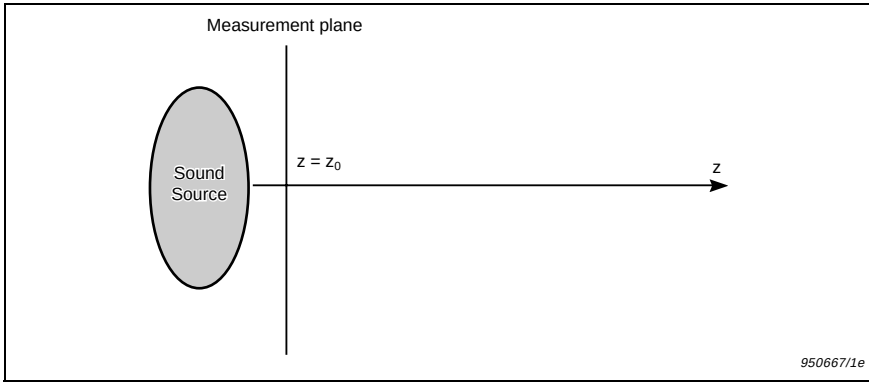

Fig. 4. Measurement geometry

The time domain sound pressure field $p(\mathbf{r}, t) = p(x, y, z, t)$ fulfils the homogeneous wave equation in the half space $z \geq 0$:

$$\nabla^2 p - \frac{1}{c^2}\frac{\partial^2 p}{\partial t^2} = 0, \quad z \geq 0 \tag{1}$$

For any given z-coordinate, we now introduce the following Fourier transform pair of the sound pressure in the three dimensions (x, y, t):

$$p(x,y,z,t) = \frac{1}{(2\pi)^3}\int_{-\infty}^{\infty}\int_{-\infty}^{\infty}\int_{-\infty}^{\infty} P(k_x,k_y,z,\omega)e^{-j(k_x x + k_y y - \omega t)}\,dk_x\,dk_y\,d\omega \qquad (2)$$

$$P(k_x,k_y,z,\omega) = \int_{-\infty}^{\infty}\int_{-\infty}^{\infty}\int_{-\infty}^{\infty} p(x,y,z,t)e^{j(k_x x + k_y y - \omega t)}\,dx\,dy\,dt \qquad (3)$$

This pair exists for any *xy*-plane with $z \geq 0$. If we insert the Fourier transform expression (2) for $p(\mathbf{r}, t)$ into the wave equation (1) and take the Fourier transform, we obtain the following one-dimensional differential equation in z:

$$\left[\frac{\partial^2}{\partial z^2} + k_z^2\right]P(k_x,k_y,z,\omega) = 0, \qquad k_z^2 \equiv k^2 - k_x^2 - k_y^2, \qquad z \geq 0 \qquad (4)$$

Here, $k \equiv \omega/c$ is the wave number, ω is the temporal angular frequency and (k_x, k_y) are the spatial angular frequencies. When all sources of the sound field are in the half space $z < 0$, then the complete solution to (4) can be written as:

$$P(k_x,k_y,z,\omega) = P(k_x,k_y,z_0,\omega)e^{-jk_z(z-z_0)}, \qquad z_0 \geq 0, \qquad z \geq 0 \qquad (5)$$

where k_z is a function of the angular frequencies (k_x, k_y, ω):

$$k_z \equiv \begin{cases} \sqrt{\left(\frac{\omega}{c}\right)^2 - k_x^2 - k_y^2} & \text{for} \quad k_x^2 + k_y^2 \leq \left(\frac{\omega}{c}\right)^2 \\ -j\sqrt{k_x^2 + k_y^2 - \left(\frac{\omega}{c}\right)^2} & \text{for} \quad k_x^2 + k_y^2 > \left(\frac{\omega}{c}\right)^2 \end{cases} \qquad (6)$$

The circle in the spatial frequency plane defined by $k_x^2 + k_y^2 = (\omega/c)^2$ is called the Radiation Circle. High spatial frequencies outside the radiation circle are seen from equation (5) and (6) to be exponentially attenuated in the direction away from the source.

Since the sound pressure field is measured in the plane $z = z_0$, the plane wave spectrum P can be obtained from equation (3) with z equal to z_0. Equations (5) and (2) then allow the sound pressure field p for any $z \geq 0$ to be calculated.

Using the acoustical equation of motion, the particle velocity vector $\mathbf{u}(\mathbf{r}, t)$ can be shown to be (see reference [1]):

$$\mathbf{u}(x,y,z,t) = \frac{1}{(2\pi)^3 \rho c} \int_{-\infty}^{\infty} \int_{-\infty}^{\infty} \int_{-\infty}^{\infty} P(k_x, k_y, z, \omega) \frac{\{k_x, k_y, k_z\}^T}{k} e^{-j(k_x x + k_y y - \omega t)} dk_x dk_y d\omega \quad (7)$$

Here, $\{\ \}^T$ represents a column matrix (a vector). Any type of filter (e.g., a frequency band filter or an order tracking filter) can be applied to the time domain pressure and the time domain particle velocity signals, and the Instantaneous Intensity vector $\mathbf{I}(\mathbf{r}, t)$ can then be obtained as the product of the two quantities:

$$\mathbf{I}(\mathbf{r},t) = p(\mathbf{r},t) \cdot \mathbf{u}(\mathbf{r},t) \quad (8)$$

Finally, averaging in Time, RPM, Shaft angle or Engine cycle intervals can be performed on the calculated time signals.

We shall see that the formulation above can be interpreted as a method based on an expansion in plane (and evanescent) waves. Equation (2) can be seen as an expression for the pressure distribution in three dimensions. If we insert equation (5) in (2), then the expression takes the form of an infinite sum (an integral) of elementary waves of the form:

$$e^{-j(k_x x + k_y y + k_z z)} \quad (9)$$

For spatial frequencies (k_x, k_y) inside the radiation circle, these elementary waves are plane waves propagating in the direction given by the unit vector $\{k_x, k_y, k_z\}^T/k$. The particle velocity distribution of that elementary plane wave is given by the vector function:

$$\frac{1}{\rho c}\, e^{-j(k_x x + k_y y + k_z z)}\, \frac{\{k_x, k_y, k_z\}^T}{k} \tag{10}$$

$\rho\, c$ being the free space impedance. The particle velocity distribution of the total sound field can now be obtained by summation of the contribution from the infinite set of plane waves, in the same way as for the pressure in equation (2). This leads directly to equation (7).

Practical implementation considerations

So far, we have assumed the pressure to be known continuously over an infinite plane and over an infinite time record. In practice we can, of course, only measure and represent discrete signals over finite windows in the three dimensions (x,y,t). If the signals are band-limited in the three dimensions, then there is no loss of information in replacing the continuous signals with sampled versions, provided the sampling intervals are sufficiently small. From equation (5) it follows that the high spatial frequencies are exponentially attenuated in the direction away from the source, and in such a way that at any non-zero distance the pressure distribution will be, in practice, spatially band-limited. In the time dimension we can make the signals band-limited through the use of anti-aliasing filters. The limited window size is more of a problem because information is lost and because it leads to spectral leakage in connection with the Fourier transform.

Various techniques exist to reduce the spatial windowing effects. The one that is usually most efficient and therefore applied in NS-STSF is the so-called *Velocity Windowing* technique, which is described in reference [4]. In this, a distribution of z-oriented particle velocity is initially calculated in a *Source Plane* which is parallel with the measurement plane and which is also close to the real source surface. All other sound field calculations are then based on that so-called *Surface Velocity* map. The Surface Velocity map covers an area with the same size as the array, so the obvious question might be, why the finite size of the Surface Velocity map does not lead to spatial windowing effects, just like the finite area of the pressure distribution measured by the array. The answer is that it does lead to spatial windowing errors, but usually much less than the pressure window in the measurement plane. This is because the particle velocity in the Source Plane will have a very small z-component outside the area of the Surface Velocity map. From the z-component of the particle velocity we can calculate all other components of the sound field according to Rayleigh's first integral formula, [1].

In the practical implementation, the three-dimensional Fourier transforms in (x,y,t) in equations (2), (3), and (7) are calculated using DFT (FFT). After the DFT transformation to the temporal and spatial frequency domains, the sound field is represented by a discrete three-dimensional data set in these frequency domains. Such a discrete data set represents a signal, which is periodic in both the time domain and in the spatial domain. When we calculate the sound field in a plane parallel with the measurement plane, the periodic spatial replica of the true measurement aperture will contribute over the entire calculation plane – also inside the area corresponding to the measurement aperture. Since the major part of this error comes from the nearest part of the first replica, and since this part is just the opposite end of the measurement aperture itself, the sound field seems to "wrap around". The method used to suppress this *Wrap Around Error* is to push the replica further away by zero-padding the measured data before the DFT. A similar Wrap Around Error will also be introduced in the time dimension, and as in the spatial dimensions it is suppressed by zero-padding.

The temporal window needs special attention in the NS-STSF application. In usual frequency analysis using FFT, a smooth temporal window – such as a Hanning window – is used to minimize the spectral leakage, without sacrificing too much spectral resolution. The focus is entirely on spectral estimation. In NS–STSF it is still important to get rather good spectral estimation, because the spatial transformations involve the use of strongly frequency dependent transfer functions, such as in equation (5). However, after the multiplication with transfer functions in the frequency domain, the data need to be transformed back to the temporal domain using inverse FFT. If, for example, a Hanning window had been used before the forward FFT, then after the inverse FFT the Hanning window would still be in effect. In order to remove this window function from the output time signals, one might attempt to divide by the same Hanning window. Close to the ends of the signals this would, however, mean division by a number close to zero. If no processing had been performed in the frequency domain, this would cause problems only in a very narrow interval at the two ends of the signals. But, the processing performed in the frequency domain will include delays, because wave propagation takes time. Signal components delayed to an end interval of the time record will be divided by a number close to zero, and therefore be amplified far too much. A good solution has been found to be a Gaussian window given by the expression:

$$w_i = e^{-\frac{1}{2}\left(a\frac{2i-I}{I}\right)^2}, \quad i = 0, 1, \ldots, (I-1), \quad a = 2.6 \tag{11}$$

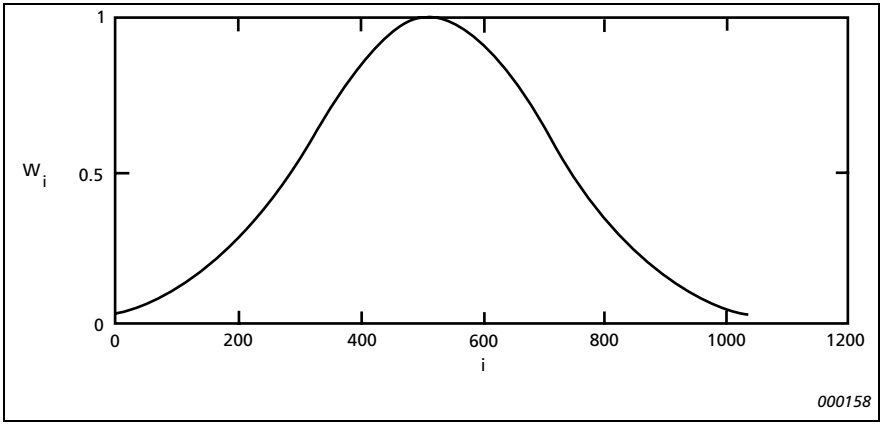

Fig. 5. Gaussian window function, shown for a 1024 sample record

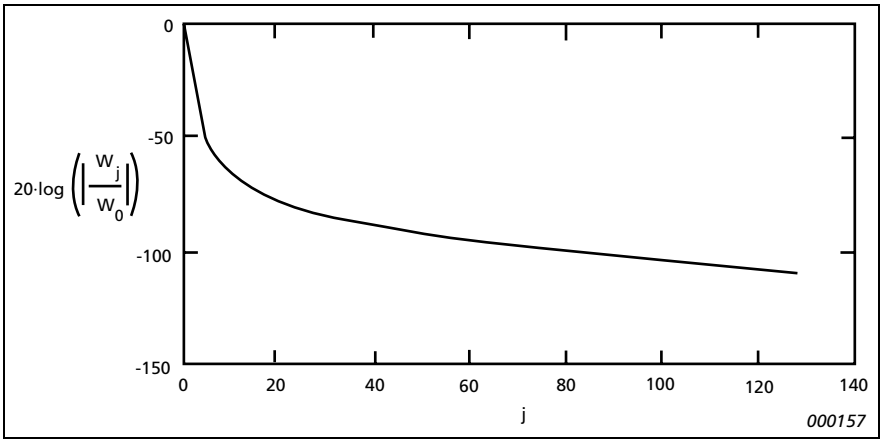

Fig. 6. Normalised spectrum of the Gaussian window function in Fig. 5, showing only the first 128 frequency lines

where I is the number of samples in the time record, [5]. The window function and its normalized FFT spectrum are shown in Fig. 5 and 6, respectively. Because the window function does not approach zero towards the ends of the record, we can divide the output time signals by the window function without getting the problem of dividing by very small numbers. Further, the

Gaussian window provides a very good combination of low spectral leakage (low side-lobe level in the window spectrum) and high spectral resolution (narrow main lobe in the window spectrum).

Interpolation of Bad Measurement Points

In some cases it is very difficult or even impossible to measure the required complete regular rectangular measurement grid. This may be due to obstacles or hazardous measurement conditions, such as high temperatures or moving parts. Another type of problem is a bad signal discovered only after a measurement has been completed. It may be then impossible or at least very expensive to re-take the measurement.

A general solution to the problem is to use an interpolation procedure capable of interpolating the sound pressure between an arbitrary set of measurement positions in a plane. This section describes a new such interpolation procedure, which is optimized to the characteristics of the sound pressure distribution over a plane at some distance from the sound sources. The method works on complex time harmonic sound pressure, so we shall look at the measured pressure $\underline{p}(x, y, z, \omega)$ after the temporal Fourier transform:

$$\underline{p}(x, y, z, \omega) \equiv \int_{-\infty}^{\infty} p(x, y, z, t) e^{-j\omega t} dt \tag{12}$$

which is part of the 3D Fourier transform in equation (3). Since for the interpolation we are concerned only with the pressure in the measurement plane $z = z_0$, we introduce a two-dimensional position vector $\mathbf{R} \equiv \{x, y\}$ in that plane. The temporal frequency domain pressure in the measurement plane can now be written as $\underline{p}(\mathbf{R}, z_0, \omega)$. For convenience we shall omit the frequency parameter ω and write just $\underline{p}(\mathbf{R})$.

We assume that the time harmonic complex sound pressure $\underline{p}(\mathbf{R}_n)$ has been measured at a set of N positions $\boldsymbol{R}_n \equiv \{x_n, y_n\}$ in the measurement plane. Without loss of generality we can restrict ourselves to estimation of the sound pressure $\underline{p}(\mathbf{0}) \equiv \underline{p}(0,0)$ at the origin. We wish to estimate $\underline{p}(\mathbf{0})$ as a linear combination of the measured sound pressure data $\underline{p}(\mathbf{R}_n)$:

$$\underline{p}(\mathbf{0}) \approx \sum_{n=1}^{N} c_n \cdot \underline{p}(\mathbf{R}_n) = \sum_{n=1}^{N} (a_n + jb_n) \cdot \underline{p}(\mathbf{R}_n) \tag{13}$$

and we wish to use a set of complex coefficients $c_n = a_n + jb_n$ that minimizes the average estimation error for typical sound fields at a distance d from the sound sources. The characteristic that we shall make use of is the spatial frequency bandwidth limitation of the sound pressure distribution in the measurement plane after the propagation over the distance $d = z_0$ from a parallel source plane. This property is described mathematically in equations (5) and (6).

In the Fourier transform pair (2) and (3), the sound pressure in the measurement plane is expressed as an infinite sum of elementary waves $e^{-j\mathbf{K}\cdot\mathbf{R}}$, where $\mathbf{K} \equiv \{k_x, k_y\}$ is a "point" in the spatial frequency domain. Notice that these waves have the same "plane wave form" in the measurement plane, no matter if the spatial frequency $\mathbf{K}$ is inside the radiation circle or outside. Only the z-dependence is very different.

Based on the above considerations, we require the linear interpolation formula (13) to provide good interpolation estimates for all the elementary waves $e^{-j\mathbf{K}\cdot\mathbf{R}}$, but with a weight $W(\mathbf{K})$ on the estimation error that depends on the attenuation of the waves over the distance d from the source surface:

$$W(\mathbf{K}) \equiv \begin{cases} 1 & |\mathbf{K}| \le k \\ e^{-d\sqrt{|\mathbf{K}|^2 - k^2}} & |\mathbf{K}| > k \end{cases} \tag{14}$$

The weighting function (14) corresponds to an assumption about identical amplitude of all spatial frequency components of the sound pressure at the source surface, see equation (5).

The estimation error in (13) for each of the elementary waves $e^{-j\mathbf{K}\cdot\mathbf{R}}$ is:

$$\varepsilon(\mathbf{c},\mathbf{K}) \equiv 1 - \sum_{n=1}^{N} c_n e^{-(j\mathbf{K}\cdot\mathbf{R}_n)} \tag{15}$$

and we define the weighted average estimation error as:

$$E(\mathbf{c}) \equiv \frac{1}{2\pi k^2}\int_0^{\infty}\int_0^{2\pi} |\varepsilon(\mathbf{c},\mathbf{K})|^2 K \, d\psi \;\; dK \tag{16}$$

where (K,ψ) are the polar coordinates of the vector $\mathbf{K}$,

$$\mathbf{K} = \{k_x, k_y\} = \{K\cos(\psi), K\sin(\psi)\} \tag{17}$$

and $\mathbf{c} = \mathbf{a} + j\mathbf{b}$ is a vector containing the complex interpolation coefficients c_n, ref. equation (13). After removal of some terms, which can be shown to equal zero, the integral expression (16) for the estimation error E reduces to:

$$E(\mathbf{a}+j\mathbf{b}) = E_0 - 2\cdot\sum_{n=1}^{N} a_n C(R_n) + \sum_{n=1}^{N}\sum_{m=1}^{N} [a_n a_m + b_n b_m] C(R_{nm}) \tag{18}$$

where $R_n \equiv |\mathbf{R}_n|$ are the distances from the estimation position to the measurement positions, $R_{nm} \equiv |\mathbf{R}_m - \mathbf{R}_n|$ are the distances between the measurement positions and:

$$E_0 \equiv \frac{1}{k^2}\int_0^{\infty} W^2(K) K \, dK \tag{19}$$

$$C(R) \equiv \frac{1}{k^2}\int_0^{\infty} W^2(K) J_0(KR) K \, dK \tag{20}$$

J_0 is the 0'th order Bessel function. We are looking for the coefficient vector $\mathbf{c} = \mathbf{a} + j\mathbf{b}$ that minimizes the average estimation error $E(\mathbf{c})$ in equation (18). The minimum of the quadratic function $E(\mathbf{c})$ is characterized by all partial derivatives being equal to zero:

$$\frac{\partial E}{\partial a_n} = 0 \quad \text{and} \quad \frac{\partial E}{\partial b_n} = 0 \tag{21}$$

which can be shown to lead to the following equations for the interpolation coefficients:

$$\sum_{m=1}^{N} C(R_{nm}) a_m = C(R_n) \qquad n = 1, 2, \ldots, N \tag{22a}$$

$$b_n = 0 \qquad n = 1,2, \ldots, N \tag{22b}$$

The minimum value $E_{\min}$ of the error $E(\mathbf{c})$ is easily shown to be:

$$E_{min} = E_0 - \sum C(R_n) a_n \tag{23}$$

In order to set up the system of linear equations in (22a), we need to calculate the integrals $C(R_{nm})$ and $C(R_n)$, the integral $C(R)$ being defined in equation (20). Here, the important part inside the radiation circle, i.e. for $|\mathbf{K}| \le k$, can be integrated analytically, and we end up with:

$$\begin{aligned} C(R) &= \frac{1}{k^2} \int_0^k J_0(KR) K dK + \frac{1}{k^2} \int_k^\infty J_0(KR) e^{-2d\sqrt{K^2 - k^2}} K dK \\ &= \frac{J_1(kR)}{kR} + \frac{1}{(2kd)^2} \int_0^\infty \left(v J_0\left(kR \sqrt{1 + \left(\frac{v}{2kd} \right)^2} \right) \right) e^{-v} dv \end{aligned} \tag{24}$$

Because of the exponential factor in the last integral, the integration interval can be truncated, and the integration can be performed by a numerical quadrature formula, such as a Gauss-Legendre formula.

By minimizing the sum-of-squares interpolation error for all the elementary (plane) waves, we have implicitly assumed no correlation between

these waves. Such a correlation would be present if, for example, the sources were assumed to be always within the area covered by the array. Slightly better interpolation could be obtained, if such a restriction could be made and exploited, but then the method would also break down if the assumption was not fulfilled.

In a practical implementation, the interpolation coefficients $\mathbf{c} = \mathbf{a}$ are not calculated for each FFT line in the temporal spectrum, because the coefficients vary slowly as a function of the frequency. Instead they are calculated at frequencies with a certain interval, and for each FFT line a frequency interpolation between the two nearest sets of coefficients is performed. Another practical aspect is a slight regularization of the coefficient matrix in the linear system of equations in formula (22a).

Envelope Active and Reactive Intensity

Having described important aspects of the holography calculations, we now turn to the post-processing. Since the output from the holography calculation is time domain data, see formulae (2), (7) and (8), we turn back to time domain instead of the temporal frequency domain.

The Instantaneous Intensity $\mathbf{I}(\mathbf{r}, t)$ consists of a Reactive part, representing spatially oscillating energy that does not carry any average acoustical energy flow, and an Active part which oscillates around a time varying local average. This time varying average is called the Envelope Active Intensity, while the time varying amplitude of the Reactive component is called the Envelope Reactive Intensity. The Active part of the Instantaneous Intensity oscillates from zero to a time varying peak value around the Envelope Active Intensity. Fig. 7 shows (in black) the oscillating Instantaneous Intensity for a measurement on broadband noise filtered to a 1/3-octave frequency band, and on top of that curve the Envelope Active Intensity is seen (in red) as a time varying local average, [6]. The dashed red curve represents the Envelope Reactive Intensity. Clearly, the Active component is much stronger than the Reactive component in this example.

Animation of a time sequence of maps of the Instantaneous Intensity $\mathbf{I}(\mathbf{r}, t)$ will provide, in many cases, an overwhelming amount of information. Since both the Active and the Reactive parts are strongly oscillating, one will often see a very complicated picture with fluctuating peaks of positive and negative Instantaneous Intensity, and it will be difficult to overview, where the Active component is strong and where predominantly Reactive intensity is

seen. The solution adopted in NS-STSF is to look at the slowly time varying Envelope Active (and Reactive) intensity.

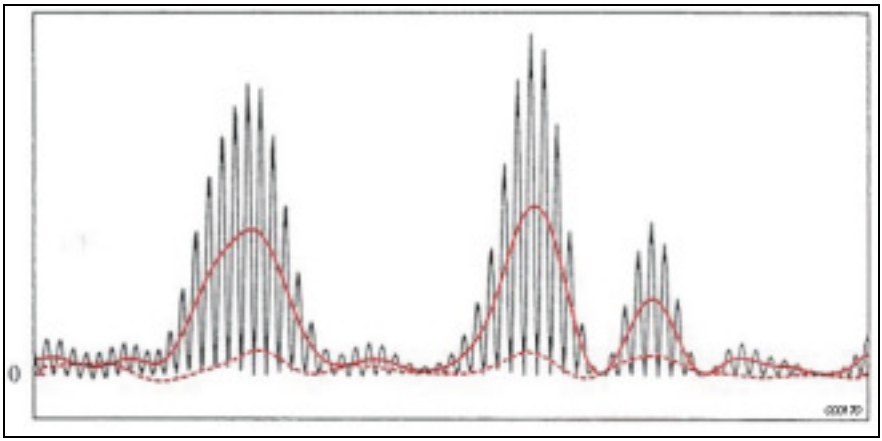

Fig. 7. Instantaneous Intensity (black), Envelope Active Intensity (red), and Envelope Reactive Intensity (red, dashed)

In order to calculate the Envelope Active Intensity $\bar{\mathbf{I}}(\mathbf{r},t)$ we need the signals $\widehat{p}\,(\mathbf{r},t)$ and $\widehat{\mathbf{u}}\,(\mathbf{r},t)$, which are Hilbert transforms in time of the pressure $p(\mathbf{r},t)$ and particle velocity vector $\mathbf{u}(\mathbf{r},t)$, respectively. A complex pressure $p_c(\mathbf{r},t)$ and a complex particle velocity vector $\mathbf{u}_c(\mathbf{r},t)$ are now defined as:

$$p_c(\mathbf{r},t) \equiv p(\mathbf{r},t) + j\,\widehat{p}\,(\mathbf{r},t) \tag{25a}$$

$$\mathbf{u}_c(\mathbf{r},t) \equiv \mathbf{u}(\mathbf{r},t) + j\,\widehat{\mathbf{u}}\,(\mathbf{r},t) \tag{25b}$$

In ref. [6], the Complex Instantaneous Intensity $\mathrm{I}_c(\mathbf{r},t)$ is then defined as:

$$\mathbf{I}_c(\mathbf{r},t) \equiv \frac{1}{2}\cdot p_c(\mathbf{r},t)\cdot \mathbf{u}_c(\mathbf{r},t)^* \tag{26}$$

where * represents a complex conjugate. The real part of this Complex Instantaneous Intensity is the Envelope Active Intensity:

$$\bar{\mathbf{I}}(\mathbf{r},t) \equiv Re\{\mathbf{I}_c(\mathbf{r},t)\} = \frac{1}{2}\cdot[p(\mathbf{r},t)\cdot\mathbf{u}(\mathbf{r},t) + \widehat{p}(\mathbf{r},t)\cdot\widehat{\mathbf{u}}(\mathbf{r},t)] \tag{27}$$

For stationary signals the overall time average of $\bar{\mathbf{I}}(\mathbf{r}, t)$ equals the overall time average of $\mathrm{I}(\mathbf{r}, t)$, [6].

Example with sinusoidal signals

Some insight can be gained by looking at sinusoidal signals at a specific position **r**. Assuming a pressure signal of the form:

$$p(t) = \cos(\omega t) \tag{28a}$$

we can split the particle velocity up in an in-phase component and an out-of-phase component:

$$u(t) = a\cos(\omega t) + r\sin(\omega t) \tag{28b}$$

which leads to the following formula for the Instantaneous Intensity:

$$\begin{aligned} I(t) &= p(t)u(t) \\ &= a\cos^2(\omega t) + r\sin(\omega t)\cos(\omega t) \\ &= \frac{1}{2}a[1+\cos(2\omega t)] + \frac{1}{2}r\sin(2\omega t) \end{aligned} \tag{29}$$

See also Fig. 8. Clearly, the in-phase velocity with amplitude a represents the Active part of the sound field – only that part carries time average intensity and it does not oscillate across zero. The out-of-phase component with amplitude r represents the Reactive part carrying no time average intensity. The Active intensity component oscillates with double frequency around the average Active intensity $\frac{1}{2}a$, while the Reactive component oscillates with double frequency around zero.

The Hilbert transforms of the pressure and velocity signals in equations (28a) and (28b) are:

$$\widehat{p}(t) = \sin(\omega t) \tag{30a}$$

$$\widehat{u}(t) = a\sin(\omega t) - r\cos(\omega t) \tag{30b}$$

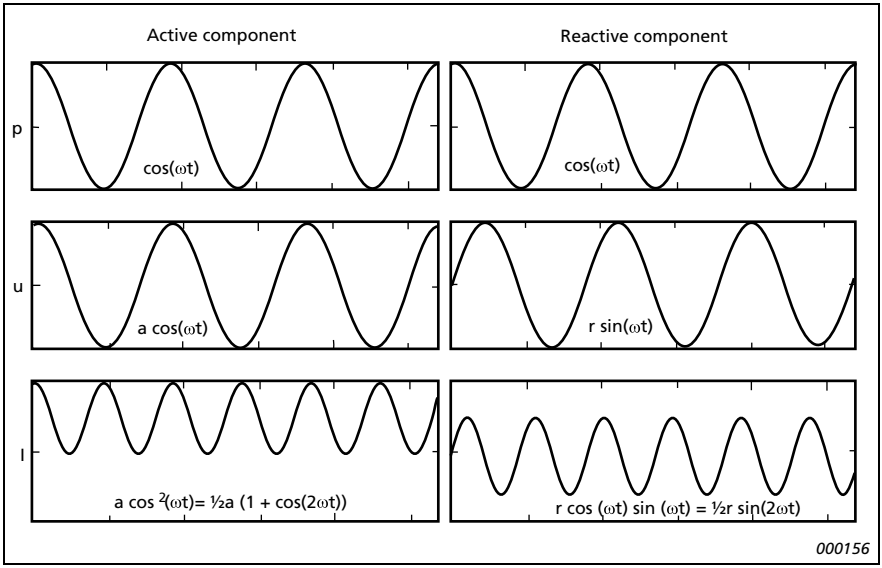

Fig. 8. Sinusoidal Active and Reactive sound field components: Instantaneous Pressure, Velocity, and Intensity

So for the complex pressure and velocity signals we obtain:

$$p_c(t) = p(t) + j\,\widehat{p}\,(t) = \cos(\omega t) + j\sin(\omega t) = e^{j\omega t} \tag{31a}$$

$$u_c(t) \equiv u(t) + j\,\widehat{u}\,(t) = ae^{j\omega t} - jre^{j\omega t} = [a - jr]e^{j\omega t} \tag{31b}$$

and thus, according to formula (26) for the complex intensity:

$$I_c(t) \equiv \bar{I}(t) + j\bar{Q}(t) = \frac{1}{2} \cdot p_c(t) \cdot u_c(t)^* = \frac{1}{2}[a + jr] \tag{32}$$

The real part of this complex intensity is the Envelope Active Intensity:

$$\bar{I}(t) \equiv Re\{I_c(t)\} = \frac{1}{2}a \tag{33a}$$

and the imaginary part is the Envelope Reactive Intensity:

$$\bar{Q}(t) \equiv Im\{I_c(t)\} = \frac{1}{2}r \tag{33b}$$

Comparing with equation (29) we see that for sinusoidal signals the Instantaneous Intensity can be written in the following form:

$$I(t) = \bar{I}[1 + \cos(2\omega t)] + \bar{Q}\sin(2\omega t) \tag{34}$$

It is apparent that the Envelope Active Intensity equals the average of the (active component of the) Instantaneous Intensity, while the Envelope Reactive Intensity is the amplitude of the reactive component of the Instantaneous Intensity.

Energy conservation property

For finite energy signals, to which group most transient signals belong, it is important to know if the Envelope Active Intensity signal $\bar{\mathbf{I}}(\mathbf{r}, t)$ represents the same energy as the Instantaneous Intensity signal $(\mathbf{r}, t)$. We define the energy vectors $\mathbf{E}$ as the time integral of the Instaneous Intensity vector signals $\mathbf{I}(\mathbf{r}, t)$. Similarly, the energy vector $\widehat{\mathbf{E}}$ is the time integral of the Instantaneous Intensity vector of the "Hilbert transformed sound field":

$$\mathbf{E} \equiv \int_{-\infty}^{\infty} \mathbf{I}(t)\,dt = \int_{-\infty}^{\infty} p(t) \cdot \mathbf{u}(t)\,dt \tag{35a}$$

$$\widehat{\mathbf{E}} \equiv \int_{-\infty}^{\infty} \widehat{p}\,(t) \cdot \widehat{\mathbf{u}}\,(t)\,dt \tag{35b}$$

Here, the dependence on the location $\mathbf{r}$ in space has been left out for simplicity. If we denote the temporal Fourier transforms of the time signals $(p, \widehat{p}, \mathbf{u}, \widehat{\mathbf{u}})$ by $(\underline{p}, \underline{\widehat{p}}, \underline{\mathbf{u}}, \underline{\widehat{\mathbf{u}}})$, then:

$$\underline{\widehat{p}}\,(\omega) = -j \cdot \mathrm{sign}(\omega) \cdot \underline{p}(\omega) \qquad \text{and} \qquad \underline{\widehat{\mathbf{u}}}\,(\omega) = -j \cdot \mathrm{sign}(\omega) \cdot \underline{\mathbf{u}}(\omega) \tag{36}$$

According to Parseval's Theorem we have:

$$\int_{-\infty}^{\infty} p \cdot \mathbf{u}\, dt = \int_{-\infty}^{\infty} \underline{p}^{*} \cdot \underline{\mathbf{u}} \frac{d\omega}{2\pi} \qquad \text{and}$$
$$\int_{-\infty}^{\infty} \widehat{p} \cdot \widehat{\mathbf{u}}\, dt = \int_{-\infty}^{\infty} \underline{\widehat{p}}^{*} \cdot \underline{\widehat{\mathbf{u}}} \frac{d\omega}{2\pi} \tag{37}$$

Using the relations given in (36) and (37) it is now easy to show that:

$$\widehat{\mathbf{E}} = \mathbf{E} \tag{38}$$

and from equations (27), (35), and (38) we finally get for the energy $\overline{\mathbf{E}}$ of the Envelope Active Intensity:

$$\overline{\mathbf{E}} \equiv \int_{-\infty}^{\infty} \bar{\mathbf{I}}(t)\, dt = \frac{1}{2} \cdot \left(\mathbf{E} + \widehat{\mathbf{E}} \right) = \mathbf{E} \tag{39}$$

Equation (39) shows that the Envelope Active Intensity signal $\bar{\mathbf{I}}(\mathbf{r},t)$ represents the same energy as the Instantaneous Intensity signal $\mathbf{I}(\mathbf{r},t)$.

Measurements

The following two sections present two NS-STSF applications, which clearly distinguish the technique from scan-based acoustical holography implementations, such as the STSF system.

Capturing and mapping a transient acoustical event

The first example that we shall consider is measurement of disc brake squeal. Since squeal noise is transient by nature and very difficult to reproduce in a controlled way, a scanning holography method is not suited. With NS-STSF a single recording is sufficient to get detailed temporal and spatial information about the squeal noise radiation.

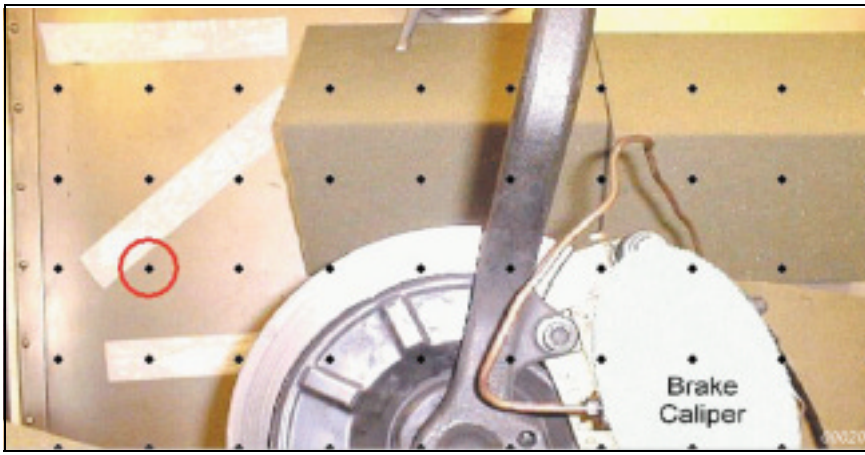

Fig. 9. Measurement area with indication of array microphone positions (dots)

Fig. 9 shows a picture of the part of the brake disc, over which the measurement was taken, and the microphone positions are indicated by dots. Because of the supporting structure it was not possible to measure the entire area of the disc. As seen in the picture, an array with 6 rows and 12 columns was used to measure the upper half of the inside of the disc. The array element spacing was 5 cm, covering a frequency range up to approximately 3 kHz, and the distance from the disc to the array was approximately 10 cm. A 4 second recording with 3.2 kHz bandwidth was made.

Clearly, the array area did not cover the entire source, as normally required. The part of the source outside the array area was shielded by absorbing material, in order to approximately meet the requirement. Further, by use of the *Velocity Windowing* technique and by the use of a smaller *Dynamic Range* than normally applied in the reconstruction of evanescent waves, quite good results were obtained.

To inspect the temporal characteristics of the recorded squeal(s), time against frequency of selected microphone signals was plotted. In Fig. 10 we have chosen the signal from the array microphone at column 3 and row 3, which is circled in Fig. 9. Clearly, the signal is dominated by a narrow-band squeal component around 2320 Hz, and the 4 second recording period is seen to contain actually three separate short squeals.

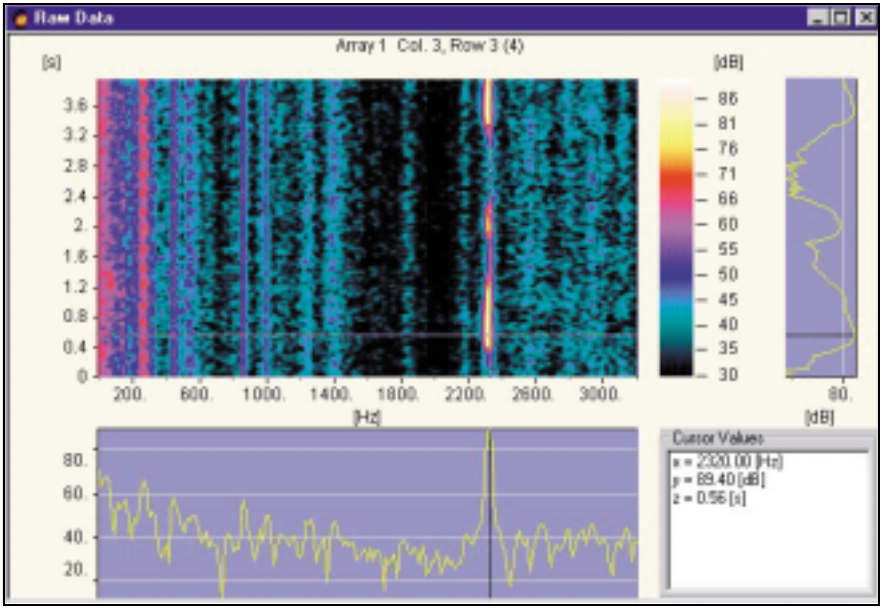

Fig. 10. Time against frequency plot in Type 7712 Raw Data view, i.e. only looking at measured signals – not calculated data

In order to calculate the sound field in some plane parallel with the array plane a Calculation Setup must be defined, see Fig. 11. The primary parameters of that setup are:

- The time and frequency interval to be processed
- The *Z*-coordinate of the calculation plane

The selection of time and frequency intervals can be based on the time against frequency plot for a selected microphone signal. Here, the same array microphone as that used in the Raw Data view in Fig. 10 has been chosen, and the time/frequency interval selected for calculation is shown as a frame on top of the contour plot. The interval is seen to cover the time and frequency intervals of the first squeal. The calculation plane has been chosen to be close to the disc.

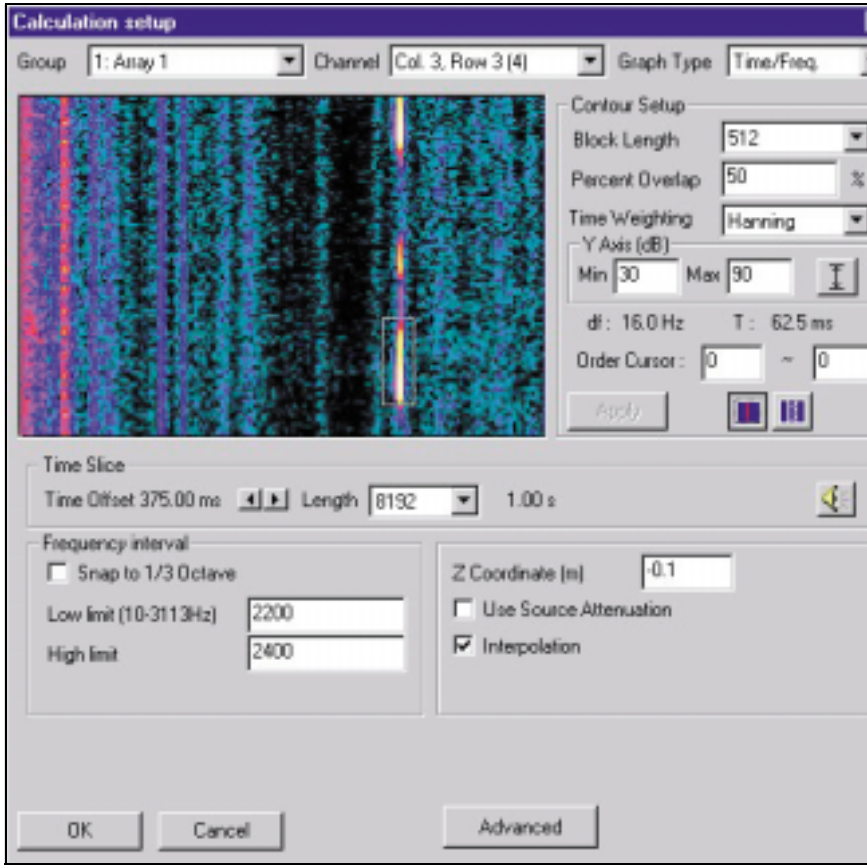

Fig. 11. Calculation Setup

Fig. 12 shows a contour plot of the Envelope Active Intensity at the point in time where the peak value is highest. For the point in space where the peak occurs, the time slice of the Envelope Active Intensity is shown in the top left corner. The time variation is seen to be very slow over the 1 second interval of the calculated time record. This is because the signal is so narrow banded.

Surprisingly, the area of highest radiation is not over the disc itself, but over a less rigid cover plate.

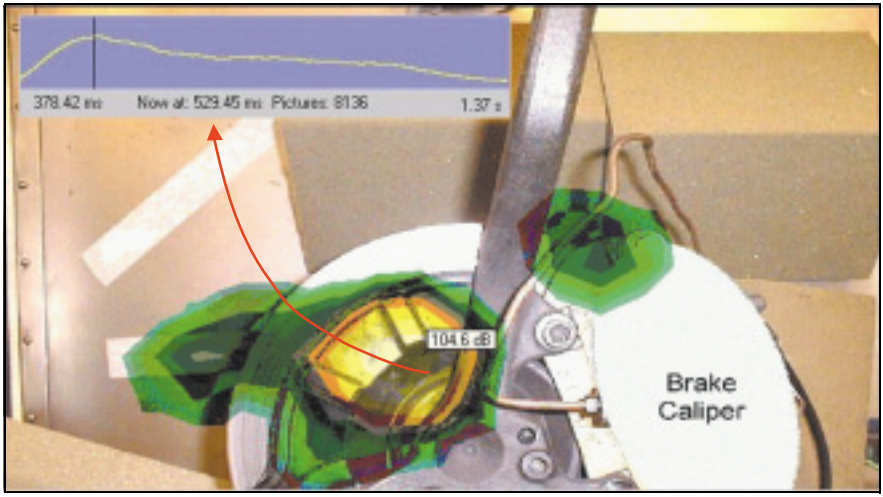

Fig. 12. Contour plot of Envelope Active Intensity. A time slice representing the position of the contour cursor is included. The contour interval is 1 dB

Analysing microphenomena and orders in engine noise radiation

Two series of measurements were taken over the Front and the Left side of a Daimler-Chrysler 2.3 litre engine, see Fig. 13. For all measurements a sampling frequency equal to 8 Ksamples per second was used, supporting a frequency range up to 3.2 kHz. Each series included the following two recordings:

1. Stationary 4000 RPM, Full Load, 2 s
2. Run-up 1000–5400 RPM, Full Load, 10 s

A main purpose of the stationary measurements was to study the sound intensity map as a function of the crankshaft angle, while the main purpose of the run-up measurements was to see the intensity map of the dominating orders at different RPM values during run-up.

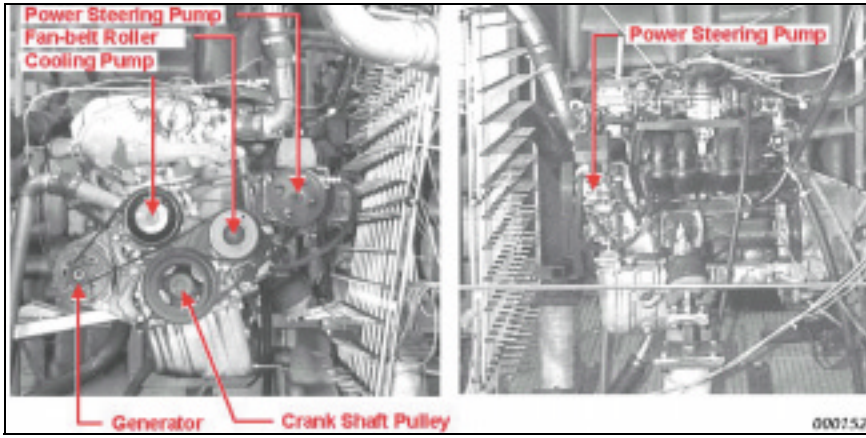

Fig. 13. Front and Left side pictures of the engine also showing the array

The measurements were taken with a 12×10 grid of Array Microphones Type 4935, i.e., there were 12 rows and 10 columns. With a grid spacing equal to 7.5 cm the supported frequency range extends up to a bit above 2 kHz. The array size of 75 cm by 90 cm was sufficient to cover the major parts of the engine. Two tacho signals were recorded together with the array signals:

1. One pulse per two rotations for definition of crank angle equal to zero
2. Two pulses per rotation for higher resolution angle definition

First we shall look at the stationary 4000 RPM measurement over the engine Front, with the purpose of studying the sound power radiation as a function of crankshaft angle.

Fig. 14 shows the Tacho Setup window, where the signals to be used for RPM and crank angle detection are selected, and also the parameters for the detection are defined. The graphics area of the window can display time signal, detected tacho sequence and RPM graph. In this case the RPM graph has been selected.

During the analysis of the measured data for the engine Front, it was discovered that the microphone in row 12 and column 9 (i.e., almost in the upper right corner) had a bad connection. The measured signal was just impulsive noise. Fortunately, we could use the Bad Measurement Interpolation function to disregard the bad signal and replace it by interpolated data. Fig. 15 shows the menu for definition of the array positions, where measured signals will be replaced by interpolated data.

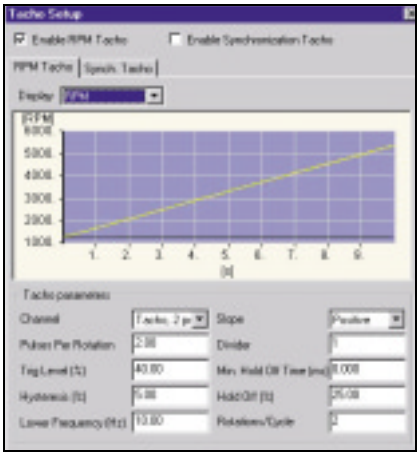

Fig. 14. Tacho Setup

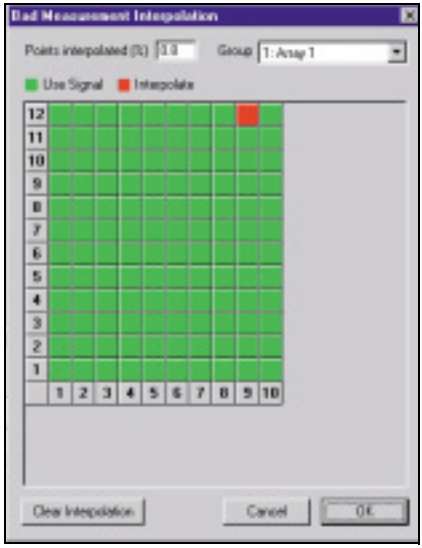

Fig. 15. Bad Measurement Interpolation

We apply a 1/3-octave filter at 1 kHz, calculate the Sound Intensity over a plane at the surface of the engine and average over 1 second. As a result we get a map of the Average Active Intensity at the engine surface as shown in Fig. 16. The areas of highest radiation are seen to be just below the crankshaft pulley and around the upper part of the fan-belt roller.

In Fig. 16 we have, of course, lost all time or crank angle resolution because of the averaging. In order to obtain time or crank angle resolution, we skip the averaging and calculate instead the Envelope Active Intensity in the same plane at the engine surface. Still we look at the 1 kHz 1/3-octave band of the stationary 4000 RPM measurement.

Fig. 17 shows from left to right four snapshots with approximately 56° crank angle interval – the crank angle being shown in the top left corner of each plot. A position cursor can be seen at the lower limitation of the crankshaft pulley, and the so-called "Properties window" below the sequence relates to that cursor position on the first plot in the sequence. The signal in the upper part of the Properties window is the (envelope Active Intensity) time signal at the position cursor. Clearly, the signal at that position is very impulsive.

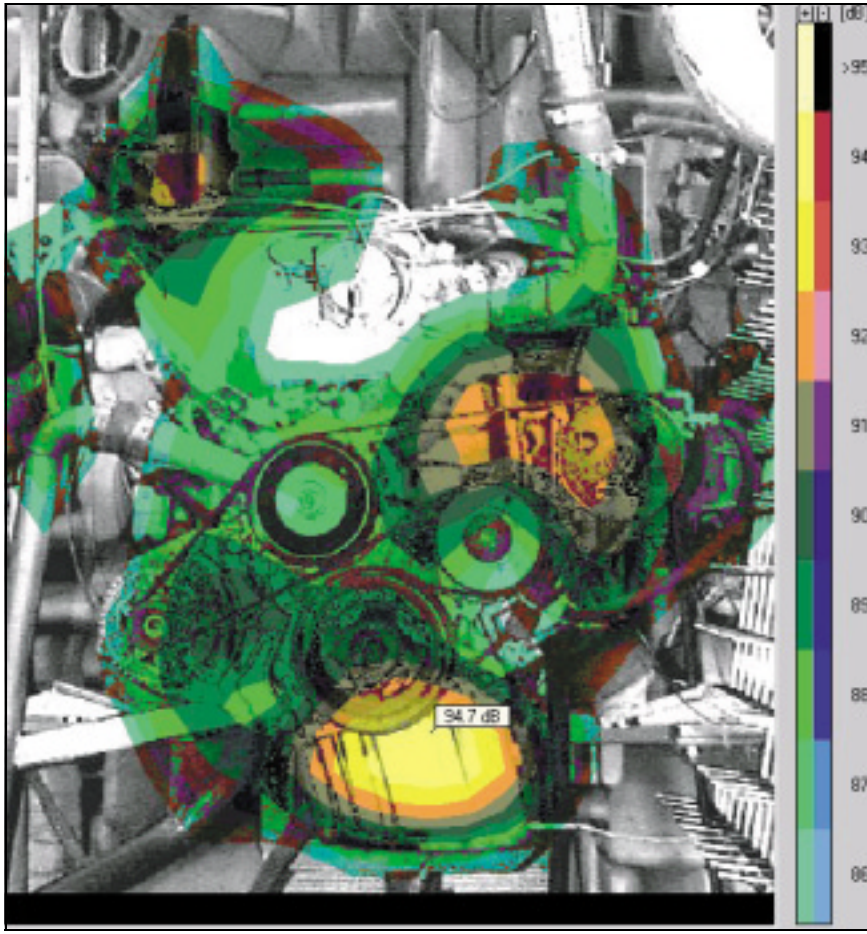

Fig. 16. Average Sound Intensity at the engine surface for the 1 kHz 1/3-octave band. The contour interval is 1 dB

A time cursor is seen in one of the impulses, indicating the instant in time represented in the contour plot. Looking again at the plot sequence, we observe that the impulse below the crankshaft pulley precedes the sound radiation from the area over and around the fan-belt roller (see Fig. 13). The impulse below the crankshaft pulley is due to the firing of the front cylinder. The cylinder pressure is transmitted through the crankshaft into the engine

block from where noise is radiated. Subsequently, the deflection propagates to other parts of the engine. The high radiation around the fan belt roller could be due to transmission through the timing belt.

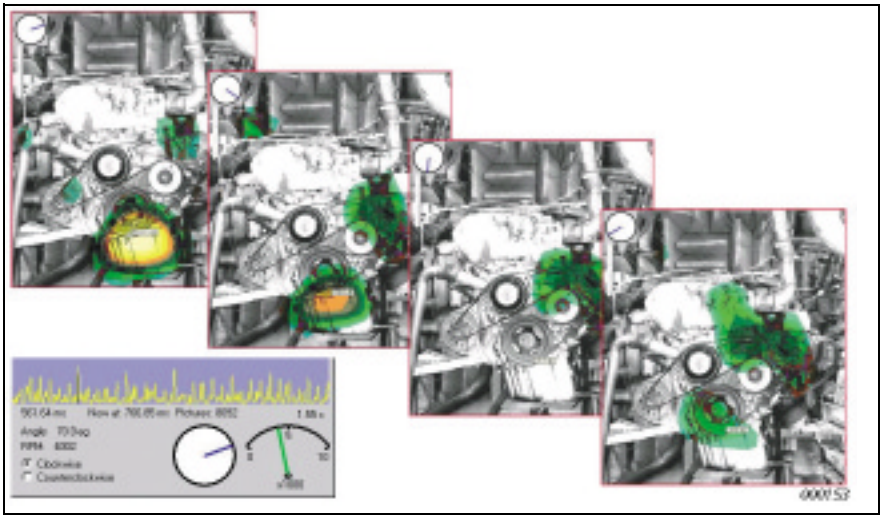

Fig. 17. Envelope Active Intensity at four different crankshaft angles and, below, the time slice at the contour cursor position. Contour interval is 1 dB

During an animation the Properties window also shows the instantaneous RPM and the corresponding crank angle. The crank angle indicators at the four instants in time represented in the plot sequence in Fig. 17 have been copied onto the four plots.

With the NS-STSF software it is very easy to search in the time/position data and to perform time animations: By clicking at a point in time, the contour plot at that time will be displayed. By clicking at a position in the contour plot, the time data for that position will be shown in the Properties window. Animation is controlled by a standard set of playback controls. Several animations can be synchronized and run in parallel.

In Fig. 17 the time slice showed a certain but not perfect periodicity of the intensity from cycle to cycle. If the aim is to obtain a good overview of the average radiation as a function of crank angle, then the time animation provides too much detailed information without giving the average picture.

To provide this overview, the NS-STSF software can perform averaging into a set of Angle Intervals of specified equal width. For the engine Front measurement we have chosen a 10° angular averaging interval width, leading to a set of 72 intervals over the 720° crankshaft rotation over a complete engine cycle.

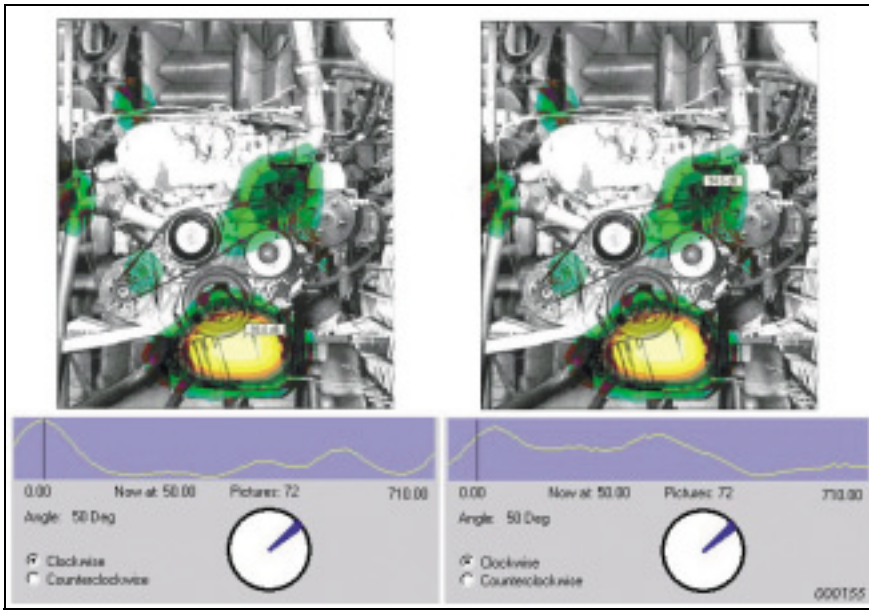

Fig. 18. 1 kHz Active Intensity averaged over a 10° crank angle 50° after the firing of the front cylinder. The crank angle slices corresponding to the two contour cursor positions are seen at the bottom. Contour interval is 1 dB

In Fig. 18 we look again at the Active Intensity in the 1 kHz 1/3-octave band, but averaged in 10° intervals. The two contour plots are identical, representing both the crank angle interval around 50° – only the cursor positions and the associated angle interval slices at the bottom are different. To the left, the contour cursor is over the oil sump, and the angle slice for that position shows that we are at the crank angle where the intensity over the oil sump is at its maximum. To the right, the contour cursor is above the fan belt roller, but we still look at the crank angle interval, where the oil sump radiation peaks. The angle slice for the position above the fan belt roller shows that

the radiation at that position peaks a bit later than the radiation from the oil sump. Another difference is that the oil sump radiation is rather concentrated in angle, whereas the radiation around the fan belt roller covers a rather broad crank angle interval.

This example illustrates the possibility of quickly reading the radiation versus crank angle at many positions by clicking the contour cursor at these positions, looking at the angle slice in the Properties window.

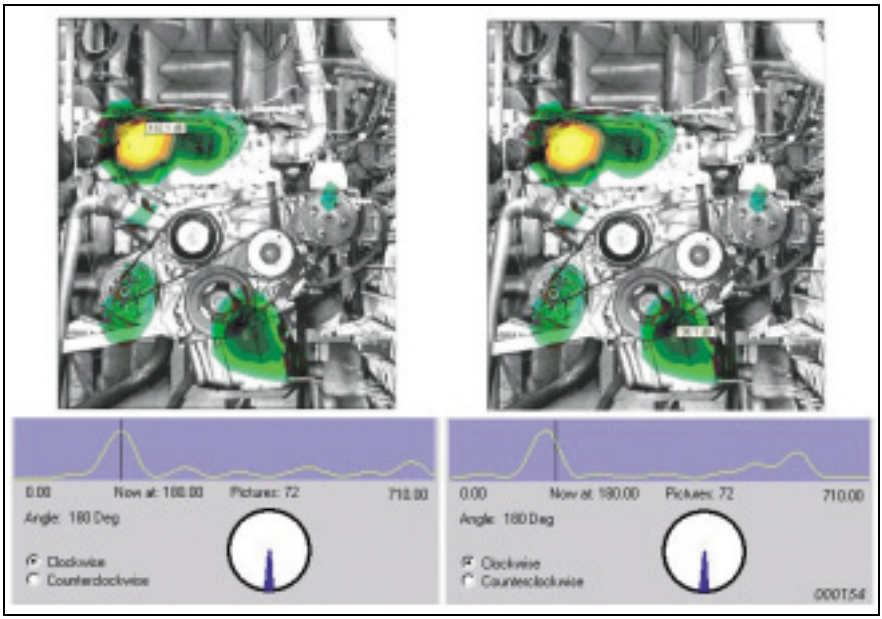

Fig. 19. 1.6 kHz Active Intensity averaged over a 10° crank angle 180° after the firing of the front cylinder. The crank angle slices corresponding to the two contour cursor positions are seen at the bootom. Contour interval is 1 dB

Fig. 19 presents the same comparison of the crank angle "timing" of two hot spots of impulsive radiation, just for the 1.6 kHz instead of the 1 kHz 1/3-octave band. Again, we have used averaging in 10° crank angle intervals, but now we look at the angle interval at 180°, i.e. approximately half a crankshaft rotation after the firing of the front cylinder.

In the Figure to the left (see Fig.19.), the contour cursor is over the valve cover, and the angle slice at the bottom shows that we are looking at the

angle, where the radiation from the valve cover peaks. Notice that most of the radiation is concentrated within a rather small angular interval. To the right we look at the same map (i.e., for the same crank angle), only the contour cursor is now over the oil sump. The angle slice for the radiation from the oil sump shows a peak before the angle cursor, i.e., before the peak radiation over the valve cover. So, apparently the impulsive radiation from the oil sump precedes the impulsive radiation from the valve cover.

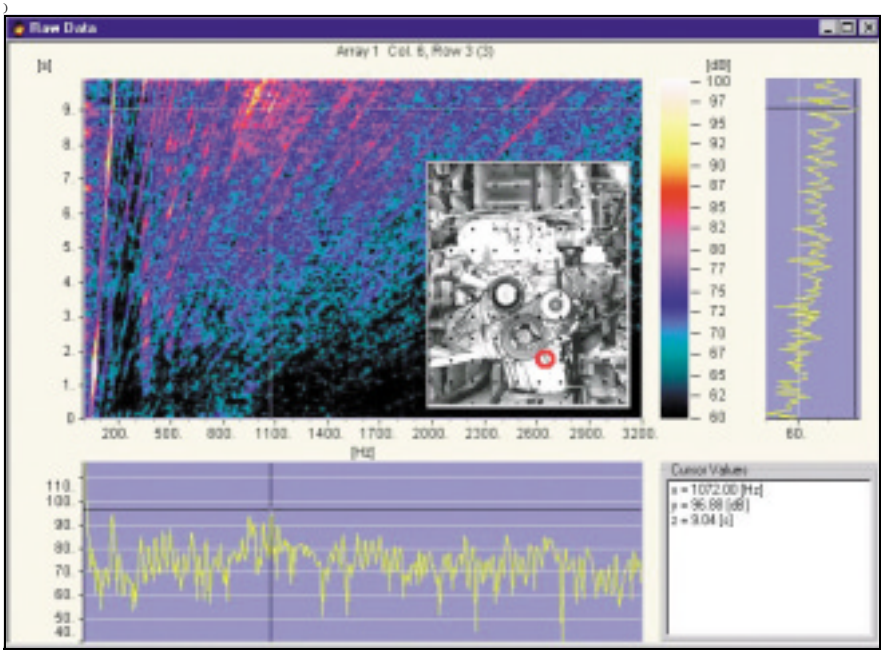

Fig. 20. Time against frequency plot of the signal from a microphone placed alongside the oil sump (red circle)

We next turn to the run-up measurements from 1000 to 5400 RPM (full load on the engine) and we shall start with the measurement over the engine Front.

A time against frequency plot of the signal from an array microphone alongside the oil sump shows a very high level of the 13th order about 1 s before the end of the 10 s recording, see Fig. 20. We will focus our attention on the 13th order.

Fig. 21 shows the Calculation Setup, where the time and frequency intervals for the processing have to be selected. To facilitate this selection, we look at the same time against frequency plot as in Fig. 20, but now the order interval between the 12.75th and the 13.25th order is shown on top of the plot. The rectangle represents the time and frequency intervals chosen for calculation – clearly the order band falls within the calculation window, which covers the run-up from 2000 to 5400 RPM.

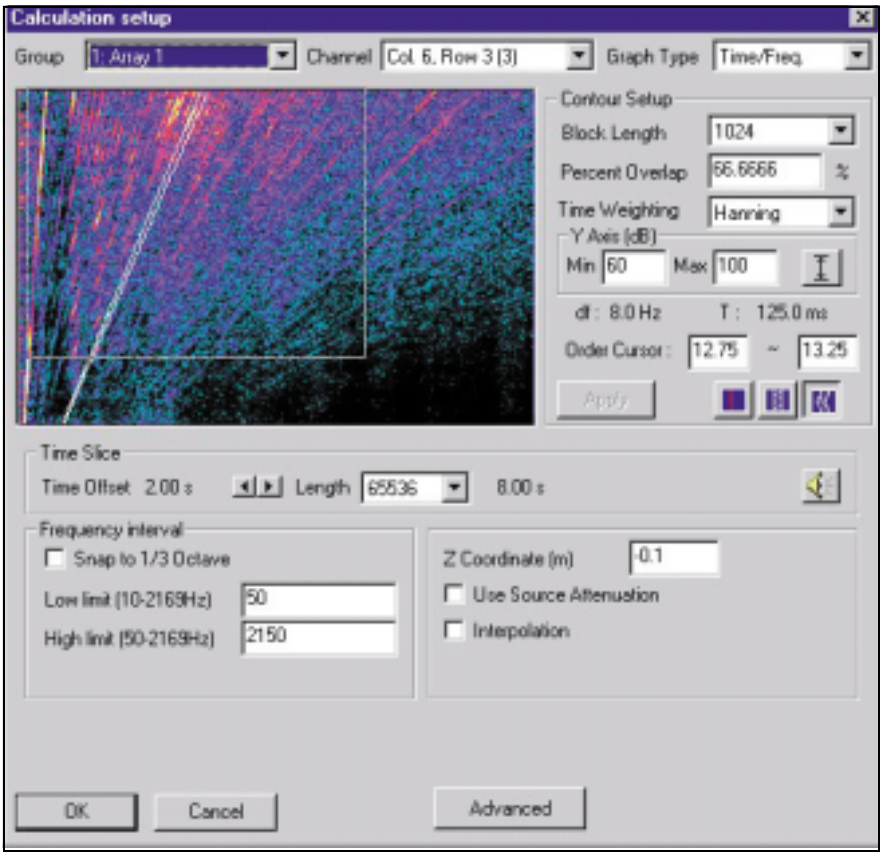

Fig. 21. Calculation Setup used with Run-up test

Again the calculation plane is chosen to be at the engine surface.

In the Display Setup we select the order filter extracting the order interval from 12.75 to 13.25, and we select averaging of Sound Intensity in RPM intervals of 100 RPM width.

As a result of the holography calculation and the averaging, we obtain a sequence of contour plots of Active Intensity covering the set of RPM intervals of 100 RPM width from 2000 to 5400 RPM. This has been done for both the Front measurement and for the measurement on the Left side.

We have then picked out the maps on the Front and Left for the RPM interval around 4950 RPM. The Properties windows below the contour plots in Fig. 22 correspond to the cursor positions in these plots, and they show slices through the RPM intervals for these cursor positions.

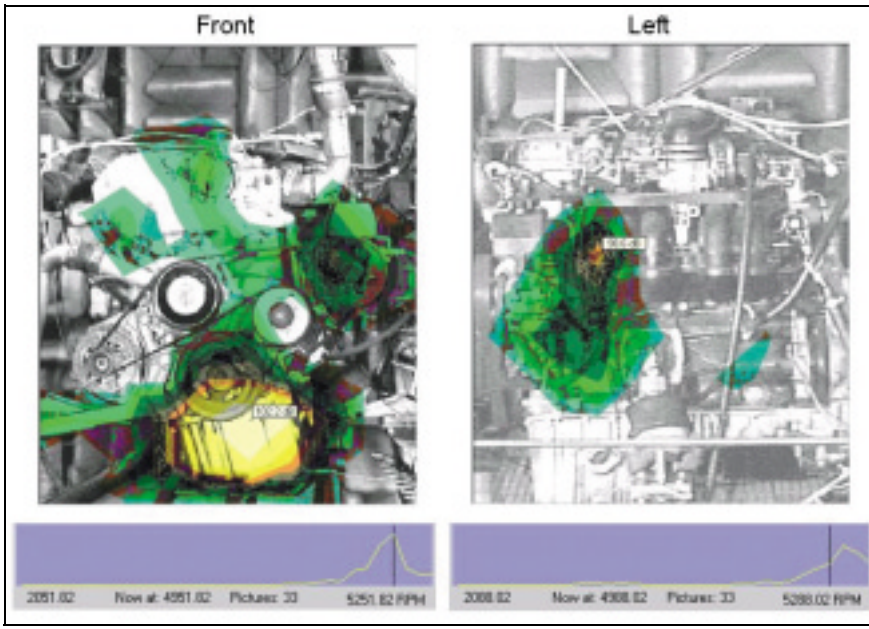

Fig. 22. Active Intensity of 13th engine Order at the Front and at the Left side of the engine. The Intensity is averaged over an interval of width 100 RPM around 4950 RPM

The dominating peak on the Front is seen to be over the oil sump, so we have positioned the contour cursor in that position. From the RPM slice under the contour plot we then see that we are looking at the RPM interval, where the

intensity level at the contour cursor position has a sharp maximum. Looking at the contour plot, a smaller peak is seen between the power steering pump and the engine block.

The dominating peak on the Left side of the engine (see Fig. 22) is between the power steering pump and the air intake manifold. From the RPM slice at that position it can be observed that the level here is actually higher in the subsequent RPM interval, i.e., around 5050 RPM.

Conclusion

Using the NS-STSF system, the sound intensity, power, pressure, velocity, and displacement maps from non-stationary noise sources can be obtained as a function of time, RPM, shaft angle or engine cycle in selected frequency or order bands. There is absolutely no restriction on the stationarity of the sound source – it can be anything from completely stationary to highly transient like a door slam. All types of output data are available as time signals (with A/D converter sample rate) or averaged in time, RPM, shaft angle or engine cycle intervals of user specified width. Looking for the hot spots in time and space of transient sound energy radiation, an overview is conveniently obtained by looking at a time varying Envelope Active Intensity map.

All the above-mentioned information is available after a single very fast time history recording with a simple microphone array.

References

[1] Maynard J.D., Williams E.G. & Lee Y., "*Nearfield acoustic holography: I. Theory of generalized holography and the development of NAH*", J. Acoust. Soc. Am., 78 (4), 1985, pp 1395 – 1413

[2] Hald J., "*STSF – a unique technique for scan-based Near-field Acoustic Holography without restrictions on coherence*", Brüel & Kjær Technical Review No.1, 1989, pp 1 – 50

[3] Saemann E.-U. & Hald J., "*Transient tyre noise measurements using Time Domain Holography*", 1997, Proc. SAE

[4] Hald J., "*Reduction of spatial windowing effects in acoustical holography*", 1994, Proceedings Inter-Noise

[5] Harris F.J., "*On the Use of Windows for Harmonic Analysis with the Discrete Fourier Transform*", Proc. IEEE, Vol. 66, No. 1, 1978, pp 51 – 83

[6] Jacobsen F., "*A note on instantaneous and time-averaged active and reactive intensity*", J. Sound Vib., 147, 1991, pp 489 – 496

Previously issued numbers of Brüel & Kjær Technical Review

(Continued from cover page 2)

4 – 1986 Field Measurements of Sound Insulation with a Battery-Operated Intensity Analyzer
Pressure Microphones for Intensity Measurements with Significantly Improved Phase Properties
Measurement of Acoustical Distance between Intensity Probe Microphones
Wind and Turbulence Noise of Turbulence Screen, Nose Cone and Sound Intensity Probe with Wind Screen

3 – 1986 A Method of Determining the Modal Frequencies of Structures with Coupled Modes
Improvement to Monoreference Modal Data by Adding an Oblique Degree of Freedom for the Reference

2 – 1986 Quality in Spectral Match of Photometric Transducers
Guide to Lighting of Urban Areas

1 – 1986 Environmental Noise Measurements

4 – 1985 Validity of Intensity Measurements in Partially Diffuse Sound Field
Influence of Tripods and Microphone Clips on the Frequency Response of Microphones

3 – 1985 The Modulation Transfer Function in Room Acoustics
RASTI: A Tool for Evaluating Auditoria

2 – 1985 Heat Stress
A New Thermal Anemometer Probe for Indoor Air Velocity Measurements

1 – 1985 Local Thermal Discomfort

Special technical literature

Brüel & Kjær publishes a variety of technical literature which can be obtained from your local Brüel & Kjær representative.

The following literature is presently available:

- Catalogue
- Product Data Sheets (English, German, French,)

Furthermore, back copies of the Technical Review can be supplied as shown in the list above. Older issues may be obtained provided they are still in stock.

BV 0053 – 11 ISSN 0007–2621

HEADQUARTERS: DK-2850 Nærum · Denmark
Telephone: +45 45 80 05 00 · Fax: +45 45 80 14 05
Internet: http://www.bksv.com · e-mail: info@bk.dk

Brüel & Kjær